Growth and electrical transport properties of La_{0.7}Sr_{0.3}MnO_{3} thin films on Sr_{2}IrO_{4} single crystals

E. J. Moon, A. F. May, P. Shafer, E. Arenholz, and S. J. May

Growth and electrical transport properties of $La_{0.7}Sr_{0.3}MnO_3$ thin films on Sr_2IrO_4 single crystals

E. J. Moon,[1] A. F. May,[2, *] P. Shafer,[3] E. Arenholz,[3] and S. J. May[1, †]

[1]*Department of Materials Science and Engineering,*
Drexel University, Philadelphia, PA 19104, USA
[2]*Materials Science and Technology Division, Oak Ridge National Laboratory, Oak Ridge, TN 37381, USA*
[3]*Advanced Light Source, Lawrence Berkeley National Laboratory; Berkeley, CA 94720, USA*

We report the physical properties of $La_{0.7}Sr_{0.3}MnO_3$ thin films on Sr_2IrO_4 single crystals. The manganite films are deposited using oxide molecular beam epitaxy on flux-grown (001)-oriented iridate crystals. Temperature-dependent magnetotransport and X-ray magnetic circular dichroism measurements reveal the presence of a ferromagnetic metallic ground state in the films, consistent with films grown on $SrTiO_3$ and $La_{0.3}Sr_{0.7}Al_{0.65}Ta_{0.35}O_3$ under a similar strain state. A parallel resistance model is used to separate conduction effects within the Sr_2IrO_4 substrate and the $La_{0.7}Sr_{0.3}MnO_3$ thin films, revealing that the measured resistance maximum does not correspond to the manganite Curie temperature but results from a convolution of properties of the near-insulating substrate and metallic film. The ability to grow and characterize epitaxial perovskites on Sr_2IrO_4 crystals enables a new route for studying magnetism at oxide interfaces in the presence of strong spin-orbit interactions.

I. INTRODUCTION

The use of epitaxial interfaces to stabilize or manipuate physical properties of materials has played a central role in condensed matter physics. In complex oxide heterostructures, considerable experimental and theoretical effort over the last two decades has focused on exploiting interfaces to realize new electronic, magnetic, superconducting and ferroelectric behavior.[1–8] The most commonly studied interface is the film/substrate junction, which is an inevitable component of all epitaxial heterostructures. By growing films on a variety of substrates, the epitaxial strain state of the film can be tuned, inducing elastic deformations to the unit cell that result in non-bulk-like rotations and/or distortions of the corner-connected BO_6 octahedra for ABO_3 perovskite films.[9–11] Additionally, mismatches in the octahedral behavior of the film and substrate can result in local changes to the B-O-B bond angle and B-O bond length in the near-interfacial region of the film/substrate heterojunction.[12–17] These substrate-imposed modifications to the film's atomic structure can lead to significant modifications to functional properties,[18,19] as well as lead to new ferroic or electronic states not observed in isocompositional bulk counterparts.[20,21]

At present, the variety of commercially available substrates for epitaxial perovskite film growth is largely limited to a few material families - titanates, aluminates, gallates, scandates - the majority of which are insulating, non-magnetic, and consist of $3d$ B-site cations or other cations with a relatively low atomic number. This last feature serves as an obstacle to studying epitaxial junctions between $3d$ and $5d$-based perovskites, the latter of which are the subject of intense current interest owing to their large spin-orbit coupling.[22–25] The presence of significant spin-orbit coupling on one side of the interface can be expected to alter magnetic and electronic behavior in the adjoined material. For example, chiral magnetic ordering and other novel spin textures have been observed in ultrathin $3d$ transition metal films on $5d$ metallic substrates due to interfacial Dzyaloshinskii-Moriya interactions.[26–28]

Understanding the effects of spin-orbit coupling on interfacial properties has motivated recent experimental studies of $Sr_{3n-1}Ir_nO_{3n+1}$-based heterostructures, which have been carried out utilizing iridate films or superlattices.[29–36] Much of this work has focused on strain effects investigated by depositing iridate films on a variety of substrates, revealing a metal-insulator transition brought about by compressive strain in $SrIrO_3$[37,38] and strain-induced changes to the band gap, Néel temperature, and optical absorption of Sr_2IrO_4.[39–41] The presence of anisotropic magnetoresistance within the Sr_2IrO_4 layer has been demonstrated in $Sr_2IrO_4/La_{0.7}Sr_{0.3}MnO_3$ bilayers arising from exchange coupling at the interface between the antiferromagnetic iridate and the ferromagnetic manganite.[42] The focus of these previous studies has been on the physical properties of the iridate layer; in contrast, there is limited understanding of how Sr_2IrO_4 alters the behavior of an adjoined layer in a heterostructure.

Here, we demonstrate the growth of manganite films on flux-grown Sr_2IrO_4 single crystals. The pseudocubic in-plane lattice parameter of Sr_2IrO_4 has been reported ranging from 3.878 Å to 3.888 Å[43–46], values between that of commonly used substrates $SrTiO_3$ (STO, $a = 3.905$ Å) and $(LaAlO_3)_{0.3}(Sr_2AlTaO_6)_{0.7}$ (LSAT, $a = 3.87$ Å). The pseudocubic lattice parameters of bulk $La_{0.7}Sr_{0.3}MnO_3$ (LSMO) is 3.881 Å.[47] Thus, Sr_2IrO_4 can provide a closely lattice matched substrate for LSMO. Additionally, unlike ABO_3 perovskites, A_2BO_4 crystals can be cleaved yielding smooth (001) faces. We first confirm that the magnetic and electronic properties of the crystals are consistent with previous reports of Sr_2IrO_4. We then report on the structural, electronic and magne-

toresistive properties of 100 unit cell thick LSMO films deposited on the crystals using molecular beam epitaxy. We demonstrate that ferromagnetic and metallic films can be realized on the Sr_2IrO_4 crystals, paving the way for future investigations of how the large spin-orbital coupling at the interface alters magnetism and magnetotransport at iridate/manganite junctions.

II. EXPERIMENTAL METHODS

Sr_2IrO_4 crystals were grown using a $SrCl_2$ flux in Pt crucibles. The starting materials $SrCO_3$, IrO_2, and $SrCl_2$ were combined in a 2:1:7 ratio, respectively. The Pt crucible was covered with a Pt lid, and heated to 1300°C. Upon reaching this maximum temperature, the furnace was slowly cooled (5-6°C/h) to 900°C, and then to room temperature at 200°C/h. Crystals were removed from the excess flux by boiling and sonicating in deionized water. This procedure resulted in the growth of crystals reaching 5 mm in dimension, with typical dimensions on the order of 1-3 mm. These growth conditions are similar to those recently reported by Sung et al.[48] In Ref. 48, the importance of minimizing dwell times at the maximum temperature was highlighted, and variations in crystal behavior with growth conditions were discussed.

To verify orientation and phase purity of the Sr_2IrO_4 crystals, x-ray diffraction data were collected on as-grown facets and on powder obtained by grinding several crystals. These data collections were performed using a PANalytical X'Pert Pro MPD with a Cu $K_{\alpha,1}$ (λ = 1.5406 Å) incident beam monochromator. Rietveld refinements were performed using FullProf.[49] Magnetization measurements on single crystals were performed in a Quantum Design Magnetic Property Measurement System, with data collected while cooling in an applied field.

LSMO thin films were grown with oxide molecule beam epitaxy in an interrupted epitaxial growth mode on STO and LSAT substrates (MTI Corporation), and single crystal Sr_2IrO_4 (SIO). The substrates were mounted adjacent to one another enabling simultaneous deposition on the crystals. The substrate temperature was held at ~ 620°C, and the ozone/oxygen mixture (~ 5 / 95%) was sourced to the substrate at a rate that yielded a chamber pressure of ~ 8 × 10^{-6} Torr. The atomic fluxes for the cation deposition and the film thickness were calibrated using Rutherford backscattering spectrometry (RBS) and x-ray reflectivity (XRR), respectively.

X-ray diffraction (XRD) measurements were taken around the 002 (pseudocubic notation) truncation rod of the film with a Rigaku Smartlab diffractometer, equipped with parabolic mirror and two bounce / axis monochromator on the incident and diffracted beams. X-ray reflectivity data was fit using the GenX program.[51] Magnetotransport properties were measured in a Quantum Design Physical Property Measurement System. Transport measurements were carried out in a four point geometry for the films on STO and LSAT. Due to the presence of

surface features such as terraces, large steps and cracks that break lateral film continuity, two point probe measurements were carried out on the LSMO/SIO samples with a lateral distance of less than approximately 0.1 mm between the contacts. Magnetoresistance measurements were carried out with the magnetic field applied perpendicular to the plane of the film ($H \parallel c$). Soft X-ray spectroscopy was performed in the Vector Magnet at beamline 4.0.2 of the Advanced Light Source. Sample geometry was 20° from grazing, and 0.3 T magnetic field was applied along the X-ray beam direction for X-ray magnetic circular dichroism (XMCD) measurements. Each XMCD curve is the average of 16 measurements in which the circular polarization of the incoming X-rays was reversed for subsequent scans. Data were collected in total electron yield mode, and normalized to the intensity of incident x-rays. The absorption intensity was further normalized to the resonant edge jump (the difference between the L_3 peak intensity and the pre-edge background) in the usual manner to allow quantitative comparisons between samples.

III. RESULTS

A. Properties of Bulk Sr_2IrO_4

The quality of a film or heterostructure is dependent on the quality of the substrate. This investigation has utilized laboratory-grown single crystals as substrates, and thus it is essential to establish the properties of these crystals and demonstrate the reproducibility of such results. As such, a variety of measurements were performed to demonstrate that the Sr_2IrO_4 crystals are indeed consistent and of high quality. In summary, from a bulk perspective, the x-ray diffraction, transport and magnetic measurements indicate that the Sr_2IrO_4 crystals utilized here as substrates appear to be of high-quality, and are generally consistent between and within different growths.

Powder x-ray diffraction data from a collection of ground single crystals are shown in Fig. 1. Rietveld refinement was performed to assess the phase purity and crystal structure, and all peaks are well accounted for using the tetragonal space group $I4_1/acd$ (number 142) reported by Crawford et al.[43] The refined lattice parameters of a=5.4928(2) Å and c=25.7990(10) Å agree well with those reported in Ref. 43, and the relevant parameter for epitaxial film growth is $a/\sqrt{2}$=3.8840 Å. While these results show sharp diffraction peaks and indicate high crystallinity, it is magnetization and transport measurements that provide a better probe of sample quality in Sr_2IrO_4.

The bulk magnetization (M) and resistance measurements shown in Fig. 2 were utilized to verify that the Sr_2IrO_4 substrates/crystals are of high quality. Growth conditions can significantly influence the magnetic response of Sr_2IrO_4, particularly by changing the oxy-
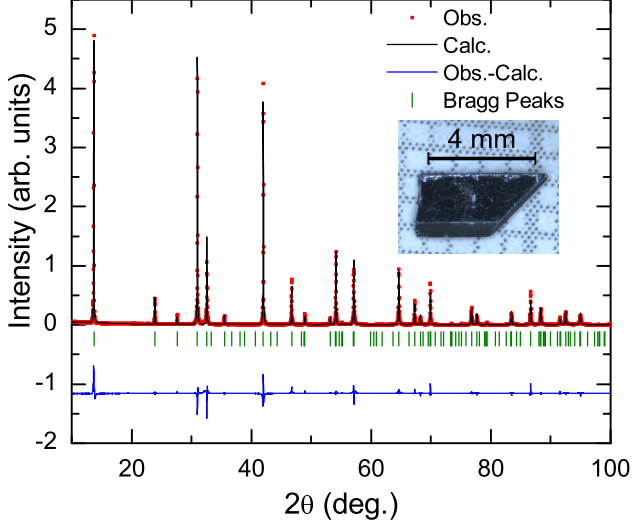
FIG. 1: (Color online) Powder x-ray diffraction data for ground crystals of Sr_2IrO_4. Rietveld refinement (labeled 'Calc') demonstrates the desired phase purity and crystal structure.
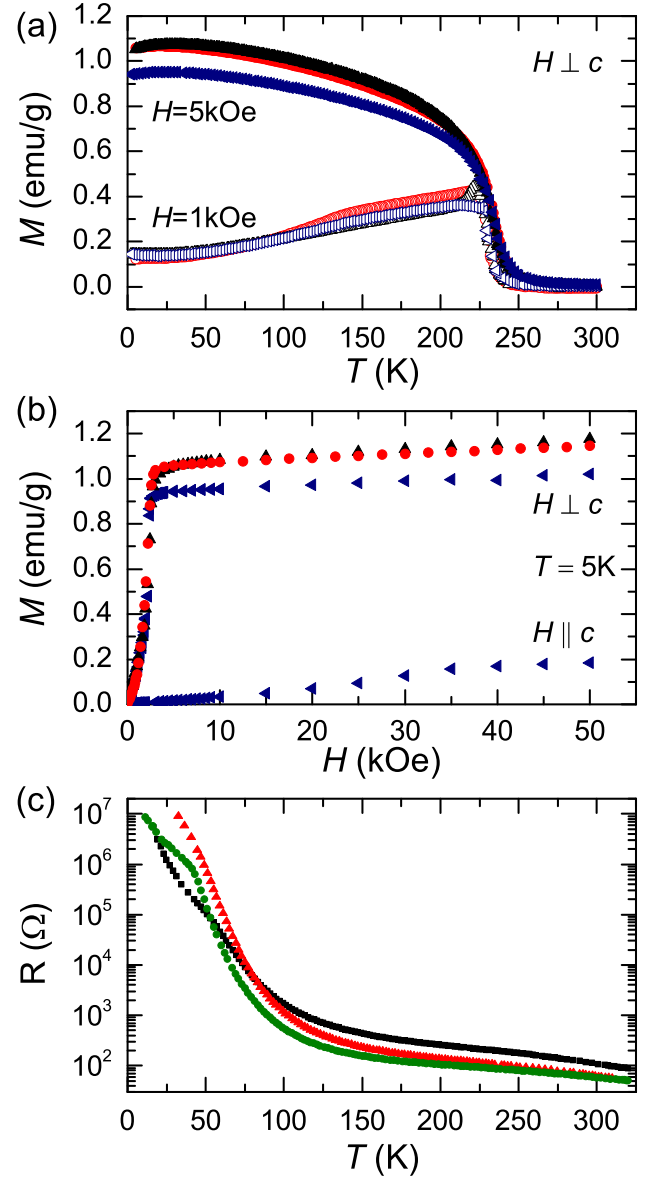

FIG. 2: (Color online) (a) Temperature dependence of the magnetization for various Sr_2IrO_4 crystals; data collected upon cooling. These panels compare the behavior observed in various samples from multiple growth batches; the crystals are found to be consistent between and within different growths. (b) Isothermal magnetization curves for single crystalline Sr_2IrO_4 demonstrating the critical field and anisotropy of the induced magnetization. (c) Electrical resistance within the ab-plane of various Sr_2IrO_4 crystals.

gen content, as was nicely demonstrated in Ref 48. The temperature-dependent magnetization data shown in Fig. 2(a) are typical for Sr_2IrO_4, which possesses a canted antiferromagnetic ground state.[50] When measuring M with a field applied within the ab plane, $M(T)$ has a cusp-like feature near 220 K if H is below the critical field of approximately 3 kOe. When H is greater than the critical field, a weak ferromagnetic state is observed due to alignment of the canted moments. As shown in Fig. 2(a), data collected with $H=5$ kOe have a temperature dependence similar to that of a ferromagnet with a Curie temperature near 240 K. The magnetic anisotropy is shown in Fig. 2(b), where isothermal magnetization scans are presented. These results show the critical field near 3 kOe for $H \perp c$, and demonstrate that the magnetization is relatively hard for $H \parallel c$. At low T, the induced moment reaches $\approx 0.08 \mu_B$/Ir (note that 1 emu/g$=0.0773 \mu_B$/Ir).

The electrical resistivity is another probe of sample quality in Sr_2IrO_4, and resistance data for representative Sr_2IrO_4 crystals are shown in Fig. 2(c). As with magnetization data, oxygen vacancies can significantly influence the temperature-dependent resistance data. In particular, oxygen vacancies promote metallic conduction in Sr_2IrO_4, and samples with the least oxygen deficiency generally appear to be the most insulating.[45] In comparison to the available literature, these Sr_2IrO_4 crystals appear to be of high quality with a large increase in resistance upon cooling. Demonstrating that the crystals become insulating at low T is important for this study, since the near-metallic state of Sr_2IrO_4 at high T provides an additional conduction path when attempting to measure the electrical properties of epitaxial films grown

on Sr_2IrO_4. The in-plane resistivity ρ_{ab} of Sr_2IrO_4 is approximately 1Ω-cm at 300 K; the resistivity along the c axis is about 2 orders of magnitude larger.[45]

B. Structural Properties of Manganite/Iridate Heterostructures

Figure 3(a) shows XRR data of LSMO films grown simultaneously on STO(001), LSAT(001), and SIO(001), respectively. The measured data were fit (solid lines) well to a model assuming a uniform scattering length density throughout film. The fits confirm the thickness of the LSMO films to be approximately 100 unit cells (uc). The reflectivity can be well fit using models with film/substrate roughness and surface roughness values of 0.2 - 0.7 nm for LSMO/STO and LSMO/LSAT; the roughness values of LSMO/SIO are larger, on order of 1.0 - 1.5 nm.

Figure 3(b) shows XRD measurements taken around the (0 0 2) (pseudocubic notation) diffraction peak of the LSMO films. The LSMO/STO and LSMO/LSAT show the expected Bragg reflection for c-axis oriented layers and clear Kiessig fringes testifying to the quality of the films. The lattice mismatch between LSMO and the various substrate materials are 0.6 % (STO), 0.1 % (SIO), and -0.3 % (LSAT), where a positive value indicates the film would be under tensile strain. The contraction of the c-axis parameters from 3.87 Å in LSMO/LSAT to 3.82 Å in LSMO/STO and LSMO/LSAT is consistent with changes in the lattice parameters that would be expected in strained films. In contrast, the film on a SIO crystal exhibits a broad peak, which is centered at 2θ = 46.8° (c = 3.882 Å). This c-axis parameter is not between that of LSMO/LSAT and LSMO/STO as would be anticipated for a strained film, suggesting that the LSMO/SIO film is at least partially relaxed.

The surface morphology of LSMO on SIO was investigated with atomic force microscopy. Images obtained from a specularly reflective region of a LSMO/SIO film are shown in Figure 3(c,d). The surface morphology of the LSMO/SIO exhibits smooth regions separated by large step heights of 3 - 4 nm. An example step is shown in Figure 3(c), along with a corresponding line scan. Figure 3(d) shows the morphology in a smooth region, where surface roughness is one unit cell or less. We assign these large steps as the origin of the increased roughness measured in XRR and the broadening of the film diffraction peak. We suggest that these steps create planar defects through the film and may also assist in strain relaxation that appears to have occurred within the film. We also note that there must exist larger steps, terraces, or cracks within the crystals that lead to lateral discontinuities within the film, as transport measurements in which the contacts were placed at distances greater than $\approx 0.1\,$mm resulted in insulating behavior dominated by the substrate, as opposed to the metallic conduction described below.
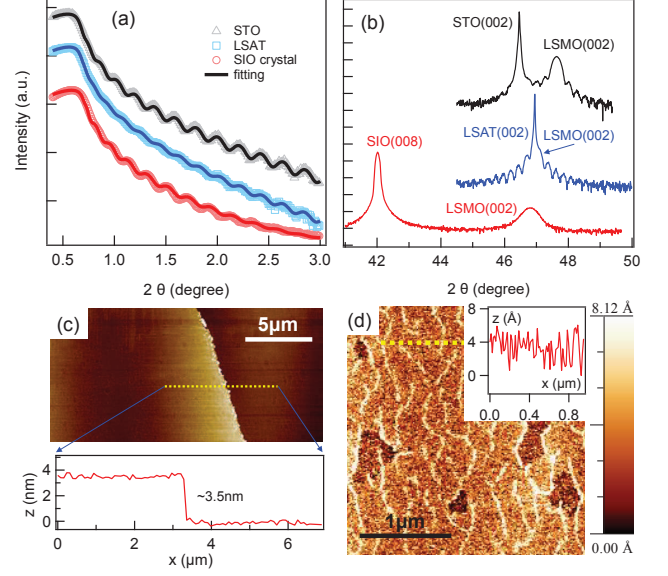

FIG. 3: (Color online) (a) X-ray reflectivity measured from LSMO films grown on STO and LSAT substrates and a SIO crystal. The solid lines are the fits to a model by GenX software. (b) X-ray diffraction measured from LSMO films on STO and LSAT substrates and a SIO crystal. (c) Atomic force microscopy image showing a step height in the LSMO/SIO film and (d) an example region between the step heights; line scan obtained from the dotted yellow lines are shown in (c) and (d).

C. Magnetotransport Properties of Manganite/Iridate Heterostructures

We next turn to DC transport measurements to elucidate the electronic properties of the films. Figure 4(a) shows the temperature dependence of the resistivity of the LSMO films grown on insulating LSAT and STO. These films are metallic, consistent with previous reported behavior of LSMO on these substrates, albeit with a local maximum at ~310 K which is reduced from the near 350 K maximum observed in optimized LSMO.[52–55] In manganites, a resistivity maximum is commonly observed at or near the Curie temperature.[56,57] The temperature dependent resistance of the LSMO/SIO sample is shown in Figure 4(b). We do not attempt to convert the LSMO/SIO measured resistance into resistivity as the SIO substrate provides a parallel conduction path to the LSMO film. In contrast to the other two films grown simultaneously, the film on SIO exhibits a maximum at ~ 250 K. To assist in interpretation of the resistance data, we modeled the resistance (R) in the LSMO/SIO as resistors in parallel using, $1/R = A_S/R_S + A_L/R_L$, where R_S and R_L are the measured resistances from the SIO crystal and LSMO film on STO, respectively, and A_S and A_L are prefactors that would arise from geometric effects. While we use the LSMO/STO resistance obtained from a four point probe resistance measurement, we show re-

sults from a two point probe measurement of the same sample in the Supplemental Materials.[58] We obtained a nearly identical temperature dependence of the resistance for these two geometries confirming that the four point resistance of LSMO on STO can be used in our parallel conduction model and that any temperature dependence to the contact resistance is a minimal effect.

This simple model reproduces the resistance maximum near 250 K when A_S and A_L to 1 are set to 1 as shown by curve A in Figure 4(c), while modifying the prefactors A_S and A_L changes the location of the resistance maximum, as shown by curves B and C. We note that the aim of this modeling is not to reproduce the exact magnitude of the resistance but instead to elucidate the nature of the local maximum in resistance. By reproducing this feature, we confirm that the resistance maximum of the LSMO/SIO arises from contributions in both the LSMO and SIO, and therefore, the measured resistance maximum does not indicate the Curie temperature or the presence of a metal-insulator transition within the film. Instead, the model indicates that the resistance of the LSMO/SIO film follows a temperature dependence that is approximately the same as the LSMO/STO film, remaining metallic up to room temperature.

In Figure 4(c), the grey line is the absolute resistance measured for LSMO/STO presented in Figure 4(a). We used this resistance to represent the resistance of the LSMO film in the two resistor model, although we note that the LSMO/STO measurement was carried out in a four point geometry and thus the effect of contact resistance is not included in the LSMO data used within the model. The data represented by black squares in Figure 2(c) was used for the SIO resistance. At 100 K, this SIO crystal is approximately 50 times more resistive than the LSMO film on STO. Thus, while the exact proportions will vary with a particular crystal, electrical resistivity measurements can be considered to be dominated by the film below approximately 100 K. Indeed, the resistance of LSMO on STO and that of the simple model A converge below ≈125 K, as shown in Figure 4(c).

Field dependent magnetoresistance (MR) measurements from the LSMO/SIO sample, shown in Figure 4(d), are also consistent with the transport occuring through the LSMO film below ≈150 K. The general field dependence of the MR curve and the reduction of MR with decreasing temperature is in agreement with previous reports of ferromagnetic manganites[59,60] and measurements of our LSMO/STO and LSMO/LSAT films. While SIO also exhibits negative magnetoresistance, the field dependence of MR in SIO is markedly different from the LSMO/SIO film, namely that bulk SIO exhibits the opposite concavity in MR as a function of field as what is shown in Figure 4(d).[46,61] In total, the measured resistance and magnetoresistance, interpreted through a parallel resistor model, indicates that the transport properties of LSMO on SIO are metallic up to temperatures of ∼310 K and that transport measurements below 125 K probe contributions from the LSMO layer with minimal
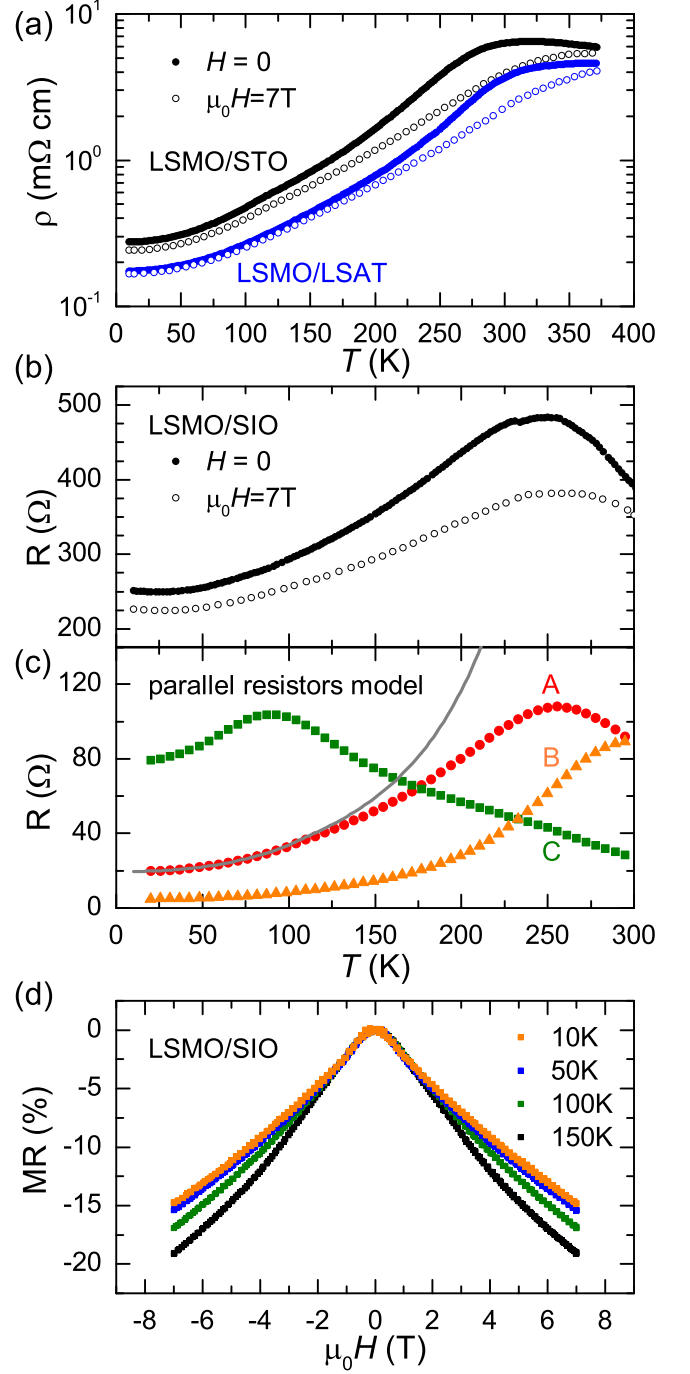

FIG. 4: (Color online) Temperature-dependent resistivity measured in zero magnetic field (filled symbols) and 7 T (open symbols) of LSMO films grown on (a) STO and LSAT substrates and (b) a SIO crystal. (c) Simulation results from the parallel resistor model obtained using $A_S = A_L = 1$ (curve A); $A_S = 1/4$, $A_L = 4$ (curve B); $A_S = 4$, $A_L = 1/4$ (curve C). The grey line in (c) is the absolute resistance measured for LSMO/STO presented in panel (a). (d) Field-dependent magnetoresistance measured from the LSMO/SIO sample.
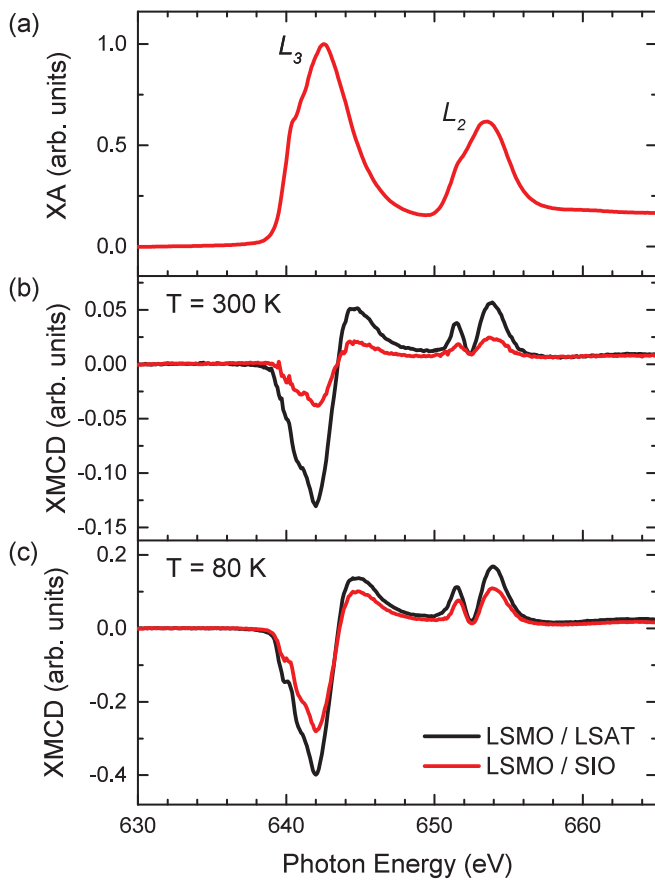
FIG. 5: (Color online) Mn L-edge x-ray absorption (XA) and XMCD of LSMO grown on SIO (red) and LSAT (black). (a) XA at 80 K; XMCD at (b) 300 K and (c) 80 K.

conduction through the SIO crystal.

The magnetic properties of the films were investigated with XMCD, in which the differences in the absorption of right and left circularly polarized X-rays were measured at the Mn L-edge. Figure 5(a) shows the Mn L-edge XMCD spectrum of a LSMO film grown on SIO (red) and LSAT (black) measured at 300 K. The presence of a XMCD signal confirms ferromagnetic ordering persists to room temperature in both samples, though their relative strength indicates a slightly lower Curie temperature for LSMO on SIO. The line shapes of the spectra are comparable to previously published data for this LSMO composition.[62–64] Furthermore, the $L_{2,3}$-edge peak position is the same for both samples, confirming that the the nominal valence of the LSMO films is independent of the substrate for films of this thickness. The presence of ferromagnetism within the LSMO/SIO sample at 300 K supports our conclusion that 100 uc thick LSMO films can be synthesized on SIO while still maintaining properties similar to LSMO/STO and LSMO/LSAT. Figure 5(b) displays the XMCD spectra at 80 K, where the difference between LSMO/SIO and LSMO/LSAT is mini-

mized compared to the 300 K data as both films are well below their Curie temperatures.

IV. DISCUSSION AND CONCLUSIONS

We have demonstrated that Sr_2IrO_4 single crystals can be used as substrates for the growth of $La_{0.7}Sr_{0.3}MnO_3$ films. The 100 uc LSMO/SIO thick films exhibit comparable electronic and magnetic properties to films deposited simultaneously on commercial STO and LSAT substrates, which in turn exhibit properties that are consistent with bulk LSMO. In contrast to the STO and LSAT substrates, the SIO crystals are not completely insulating and act as a parallel channel for conduction in the LSMO/SIO heterostructures. We have shown that the experimentally obtained transport data from LSMO/SIO can be reproduced using a parallel resistor model, allowing us to conclude that the resistivity within the LSMO film remains metallic to temperatures well above the measured resistivity maximum from the LSMO/SIO heterostructure. These results are corroborated by XMCD measurements confirming the LSMO/SIO film is ferromagnetic at room temperature.

The ability to grow epitaxial perovskite films on single crystal Sr_2IrO_4 enables a new approach for studying interfaces between $3d$ and $5d$ complex oxides, which to date have been fabricated using SIO layers grown by thin film deposition techniques. The use of SIO crystals as substrates allows for detailed characterization of the iridate prior to interface formation in order to confirm that the properties of the SIO are consistent with high quality, stoichiometric bulk crystals. Starting with a well characterized SIO crystal should enable better identification of intrinsic interfacial phenomen at SIO-based heterojunctions as opposed to defect-induced extrinsic behavior. We anticipate that epitaxial films on SIO crystals will provide a useful platform for exploring chiral magnetic states and novel spin textures in ultrathin magnetic oxide films, a topic that has attracted considerable interest in metallic magnetic interfaces but remains largely unexplored in oxide heterostructures.[65]

V. ACKNOWLEDGMENTS

[*] Electronic address: mayaf@ornl.gov

[†] Electronic address: smay@coe.drexel.edu

[1] H. Y. Hwang, Y. Iwasa, M. Kawasaki, B. Keimer, N. Nagaosa, and Y. Tokura, Nature Mat. **11**, 103 (2012).

[2] K. S. Takahashi, M. Kawasaki, and Y. Tokura, Appl. Phys. Lett. **79**, 1324 (2001).

[3] A. Ohtomo, D. A. Muller, J. L. Grazul, and H. Y. Hwang, Nature, **419**, 378 (2002).

[4] A. Gozar, G. Logvenov, L. Fitting Kourkoutis, A. T. Bollinger, L. A. Giannuzzi, D. A. Muller, and I. Bozovic, Nature **455**, 782 (2008).

[5] E. Bousquet, M. Dawber, N. Stucki, C. Lichtensteiger, P. Hermet, S. Gariglio, J. M. Triscone, and P. Ghosez, Nature **452**, 732 (2008).

[6] B. Jalan, S. Stemmer, S. Mack, and S. J. Allen, Phys. Rev. B **82**, 081103(R) (2010).

[7] J. M. Rondinelli and C. J. Fennie, Adv. Mater. **24**, 1961 (2012).

[8] A. Bhattacharya and S. J. May, Annu. Rev. Mater. Res. **44**, 65 (2014).

[9] D. G. Schlom, L.-Q. Chen, C. J. Fennie, V. Gopalan, D. A. Muller, X. Pan, R. Ramesh, and R. Uecker, MRS Bull. **39**, 118 (2014).

[10] S. J. May, J.-W. Kim, J. M. Rondinelli, E. Karapetrova, N. A. Spaldin, A. Bhattacharya, and P. J. Ryan, Phys. Rev. B **82**, 014110 (2010).

[11] R. L. Johnson-Wilke, D. Marincel, S. Zhu, M. P. Warusawithana, A. Hatt, J. Sayre, K. T. Delaney, R. Engel-Herbert, C. M. Schlepütz, J.-W. Kim, V. Gopalan, N. A. Spaldin, D. G. Schlom, P. J. Ryan, and S. Trolier-McKinstry, Phys. Rev. B **88**, 174101 (2013).

[12] C. L. Jia, S. B. Mi, M. Faley, U. Poppe, J. Schubert, and K. Urban, Phys. Rev. B **79**, 081405 (2009).

[13] A. Y. Borisevich, H. J. Chang, M. Huijben, M. P. Oxley, S. Okamoto, M. K. Niranjan, J. D. Burton, E. Y. Tsymbal, Y. H. Chu, P. Yu, et al., Phys. Rev. Lett. **105**, 087204 (2010).

[14] J. M. Rondinelli, S. J. May, and J. W. Freeland, MRS Bull. **37**, 261 (2012).

[15] R. Aso, D. Kan, Y. Shimakawa, and H. Kurata, Cryst. Growth & Des. **14**, 2128 (2014).

[16] T. T. Fister, H. Zhou, Z. Luo, S. S. A. Seo, S. O. Hruszkewycz, D. L. Proffit, J. A. Eastman, P. H. Fuoss, P. M. Baldo, H. N. Lee, and D. D. Fong, APL Mater. **2**, 021102 (2014).

[17] A. Vailionis, H. Boschker, Z. Liao, J. R. A. Smit, G. Rijnders, M. Huijben, and G. Koster, Appl. Phys. Lett. **105**, 131906 (2014).

[18] E. J. Moon, P. V. Balachandran, B. J. Kirby, D. J. Keavney, R. J. Sichel-Tissot, C. M. Schlepütz, E. Karapetrova, X. M. Cheng, J. M. Rondinelli, and S. J. May, Nano Lett. **14**, 2509 (2014).

[19] M. D. Biegalski, Y. Takamura, A. Mehta, Z. Gai, S. V. Kalinin, H. Ambaye, V. Lauter, D. Fong, S. T. Pantelides, Y. M. Kim, J. He, A. Borisevich, W. Siemons, and H. M. Christen, Adv. Mater. Interfaces **1** 1400203 (2014).

[20] J. H. Haeni, P. Irvin, W. Chang, R. Uecker, P. Reiche, Y. L. Li, S. Choudhury, W. Tian, M. E. Hawley, B. Craigo, A. K. Tagantsev, X. Q. Pan, S. K. Streiffer, L. Q. Chen, S. W. Kirchoefer, J. Levy, and D. G. Schlom, Nature **430**, 758 (2004).

[21] J. H. Lee, L. Fang, E. Vlahos, X. Ke, Y. W. Jung, L. Fitting Kourkoutis, J.-W. Kim, P. J. Ryan, T. Heeg, M. Roeckerath, V. Goian, M. Bernhagen, R. Uecker, P. C. Hammel, K. M. Rabe, S. Kamba, J. Schubert, J. W. Freeland, D. A. Muller, C. J. Fennie, P. Schiffer, V. Gopalan, E. Johnston-Halperin, and D. G. Schlom, Nature **466**, 954 (2010).

[22] B. J. Kim, H. Jin, S. J. Moon, J.-Y. Kim, B.-G. Park, C. S. Leem, Jaejun Yu, T.W. Noh, C. Kim, S.-J. Oh, J.-H. Park, V. Durairaj, G. Cao, and E. Rotenberg, Phys. Rev. Lett. **101**, 076402 (2008).

[23] G. Jackeli and G. Khaliullin, Phys. Rev. Lett. **102**, 017205 (2009).

[24] J.W. Kim, Y. Choi, Jungho Kim, J. F. Mitchell, G. Jackeli, M. Daghofer, J. van den Brink, G. Khaliullin, and B. J. Kim, Phys. Rev. Lett. **109**, 037204 (2012).

[25] S. Calder, J. W. Kim, G.-X. Cao, C. Cantoni, A. F. May, H. B. Cao, A. A. Aczel, M. Matsuda, Y. Choi, D. Haskel, B. C. Sales, D. Mandrus, M. D. Lumsden, and A. D. Christianson, Phys. Rev. B **92**, 165128 (2015).

[26] M. Bode, M. Heide, K. von Bergmann, P. Ferriani, S. Heinze, G. Bihlmayer, A. Kubetzka, O. Pietzsch, S. Blugel and R. Wiesendanger, Nature **447**, 190 (2007).

[27] S. Heinze, K. von Bergmann, M. Menzel, J. Brede, A. Kubetzka, R. Wiesendanger, G. Bihlmayer and S. Blgel, Nat. Phys. **7**, 713 (2011)

[28] K.-W. Kim, H.-W. Lee, K.-J. Lee, and M. D. Stiles, Phys. Rev. Lett. **111**, 216601 (2013).

[29] J. S. Lee, Y. Krockenberger, K. S. Takahashi, M. Kawasaki, and Y. Tokura, Phys. Rev. B **85**, 035101 (2012).

[30] M. Uchida, Y. F. Nie, P. D. C. King, C. H. Kim, C. J. Fennie, D. G. Schlom, and K. M. Shen, Phys. Rev. B **90**, 075142 (2014).

[31] C. Lu, A. Quindeau, H. Deniz, D. Preziosi, D. Hesse, and Marin Alexe, Appl. Phys. Lett. **105**, 082407 (2014).

[32] Y. F. Nie, P. D. C. King, C. H. Kim, M. Uchida, H. I. Wei, B. D. Faeth, J. P. Ruf, J. P. C. Ruff, L. Xie, X. Pan, C. J. Fennie, D. G. Schlom, and K. M. Shen, Phys. Rev. Lett. **114**, 016401 (2015).

[33] D. Hirai, J. Matsuno, and H. Takagi, APL Mater. **3**, 041508 (2015).

[34] J. Matsuno, K. Ihara, S. Yamamura, H. Wadati, K. Ishii, V. V. Shankar, Hae-Young Kee, and H. Takagi, Phys. Rev. Lett. **114**, 247209 (2015).

[35] J. Liu, D. Kriegner, L. Horak, D. Puggioni, C. Rayan Serrao, R. Chen, D. Yi, C. Frontera, V. Holy, A. Vishwanath, J. M. Rondinelli, X. Marti, and R. Ramesh, Phys. Rev. B **93**, 085118 (2016).

[36] T. J. Anderson, S. Ryu, H. Zhou, L. Xie, J. P. Podkaminer, Y. Ma, J. Irwin, X. Q. Pan, M. S. Rzchowski, and C. B. Eom, Appl. Phys. Lett. **108**, 151604 (2016).

[37] A. Biswas, K.-S. Kim, and Y. H. Jeong, J. Appl. Phys. **116**, 213704 (2014).

[38] L. Zhang, Q. Liang, Y. Xiong, B. Zhang, L. Gao, H. Li, Y. B. Chen, J. Zhou, S.-T. Zhang, Z.-B. Gu, S.-H. Yao, Z. Wang, Y. Lin, and Y.-F. Chen, Phys. Rev. B **91**, 035110 (2015).

[39] C. Rayan Serrao, Jian Liu, J. T. Heron, G. Singh-Bhalla, A. Yadav, S. J. Suresha, R. J. Paull, D. Yi, J.-H. Chu, M. Trassin, A. Vishwanath, E. Arenholz, C. Frontera, J. Železný, T. Jungwirth, X. Marti, and R. Ramesh, Phys.

Rev. B **87**, 085121 (2013).

[40] J. Nichols, J. Terzic, E. G. Bittle, O. B. Korneta, L. E. De Long, J. W. Brill, G. Cao, and S. S. A. Seo, Appl. Phys. Lett. **102**, 141908 (2013).

[41] A. Lupascu, J. P. Clancy, H. Gretarsson, Zixin Nie, J. Nichols, J. Terzic, G. Cao, S. S. A. Seo, Z. Islam, M. H. Upton, Jungho Kim, D. Casa, T. Gog, A. H. Said, Vamshi M. Katukuri, H. Stoll, L. Hozoi, J. van den Brink, and Y.-J. Kim, Phys. Rev. Lett. **112**, 147201 (2014).

[42] I. Fina, X. Marti, D. Yi, J. Liu, J.H. Chu, C. Rayan-Serrao, S. Suresha, A.B. Shick, J. Železný, T. Jungwirth, J. Fontcuberta and R. Ramesh, Nat. Commun. **5**, 4671 (2014).

[43] M. K. Crawford, M. A. Subramanian, R. L. Harlow, J. A. Fernandez-Baca, Z. R. Wang, and D. C. Johnston, Phys. Rev. B **49**, 9198 (1994).

[44] T. Shimura, Y. Inaguma, T. Nakamura, M. Itoh, and Y. Morii, Phys. Rev. B **52** 9143, (1995).

[45] O. B. Korneta, Tongfei Qi, S. Chikara, S. Parkin, L. E. De Long, P. Schlottmann, and G. Cao, Phys. Rev. B **82**, 115117 (2010).

[46] X. Chen, T. Hogan, D. Walkup, W. Zhou, M. Pokharel, M. Yao, W. Tian, T. Z. Ward, Y. Zhao, D. Parshall, C. Opeil, J. W. Lynn, V. Madhavan, and S. D. Wilson, Phys. Rev. B **92**, 075125 (2015).

[47] P. G. Radaelli, G. Iannone, M. Marezio, H. Y. Hwang, S.-W. Cheong, J. D. Jorgensen, and D. N. Argyriou, Phys. Rev. B **56**, 8265 (1997).

[48] N. H. Sung, H. Gretarsson, D. Proepper, J. Porras, M. Le Tacon, A. V. Boris, B. Keimer and B. J. Kim, Philos. Mag. **96**, 413 (2016).

[49] J. Rodríguez-Carvajal, Physica B **192**, 55 (1993).

[50] B. J. Kim, H. Ohsumi, T. Komesu, S. Sakai, T. Morita, H. Takagi, and T. Arima, Science **3232**, 1329 (2009).

[51] M. Björck and G. Andersson, J. Appl. Crystallogr. **40**, 1174 (2007).

[52] Y. Takamura, R. V. Chopdekar, E. Arenholz, and Y. Suzuki, Appl. Phys. Lett. **92**, 162504 (2008).

[53] A. Bhattacharya, S. J. May, S. G. E. te Velthuis, M. Warusawithana, X. Zhai, Bin Jiang, J.-M. Zuo, M. R. Fitzsimmons, S. D. Bader, and J. N. Eckstein, Phys. Rev. Lett. **100**, 257203 (2008).

[54] C. Adamo, X. Ke, P. Schiffer, A. Soukiassian, M. Warusawithana, L. Maritato, and D. G. Schlom, Appl. Phys. Lett. **92**, 112508 (2008).

[55] H. Boschker, M. Huijben, A. Vailionis, J. Verbeeck, S. van Aert, M. Luysberg, S. Bals, G. van Tendeloo, E. P. Houwman, G. Koster, D. H. A. Blank and G. Rijnders, J. Phys. D: Appl. Phys. **44**, 205001 (2011).

[56] A. Urushibara, Y. Moritomo, T. Arima, A. Asamitsu, G. Kido, and Y. Tokura, Phys. Rev. B **51**, 14103 (1995).

[57] J.-B. Yau, X. Hong, A. Posadas, C. H. Ahn, W. Gao, E. Altman, Y. Bason, L. Klein, M. Sidorov, and Z. Krivokapic, J. Appl. Phys. **102**, 103901 (2007).

[58] See Supplemental Material at [URL will be inserted by publisher] for comparison of two and four point probe resistance measurements of LSMO/STO.

[59] M. F. Hundley, M. Hawley, R. H. Heffner, Q. X. Jia, J. J. Neumeier, J. Tesmer, J. D. Thompson, and X. D. Wu, Appl. Phys. Lett. **67**, 860 (1995).

[60] Y. Tokura and Y. Tomioka, J. Magn. Magn. Mater. **200**, 1 (1999).

[61] M. Ge, T. F. Qi, O. B. Korneta, D. E. De Long, P. Schlottmann, W. P. Crummett, and G. Cao, Phys. Rev. B **84**, 100402(R) (2011).

[62] J.-H. Park, E. Vescovo, H.-J. Kim, C. Kwon, R. Ramesh, and T. Venkatesan, Phys. Rev. Lett. **81**, 1953 (1998).

[63] J. J. Kavich, M. P. Warusawithana, J. W. Freeland, P. Ryan, X. Zhai, R. H. Kodama, and J. N. Eckstein, Phys. Rev. B **76**, 014410 (2007).

[64] F. Yang, N. Kemik, M. D. Biegalski, H. M. Christen, E. Arenholz, and Y. Takamura, Appl. Phys. Lett. **97**, 092503 (2010).

[65] F. Hellman, A. Hoffmann, Y. Tserkovnyak, G. S. D. Beach, E. E. Fullerton, C. Leighton, A. H. MacDonald, D. C. Ralph, D. A. Arena, H. A. Dürr, P. Fischer, J. Grollier, J. P. Heremans, T. Jungwirth, A. V. Kimel, B. Koopmans, I. N. Krivorotov, S. J. May, A. K. Petford-Long, J. M. Rondinelli, N. Samarth, I. K. Schuller, A. N. Slavin, M. D. Stiles, O. Tchernyshyov, A. Thiaville, B. L. Zink, arXiv:1607.00439.